

Highly Luminescent $\text{Zn}_x\text{Cd}_{1-x}\text{Se}/\text{C}$ Core/Shell Nanocrystals: Large Scale Synthesis, Structural and Cathodoluminescence Studies

Sayan Bhattacharyya,[†] Yevgeni Estrin,[‡] Ofer Moshe,[‡] Daniel H. Rich,[‡] Leonid A. Solovyov,[§] and A. Gedanken^{†,*}

[†]Department of Chemistry and Kanbar Laboratory for Nanomaterials at the Bar-Ilan University Center for Advanced Materials and Nanotechnology, Bar-Ilan University, Ramat-Gan 52900, Israel, [‡]Department of Physics, The Ilse Katz Institute for Nanoscience and Nanotechnology, Ben-Gurion University of the Negev, P.O.Box 653, Beer-Sheva 84105, Israel, and [§]Institute of Chemistry and Chemical Technology, 660049 Krasnoyarsk, Russia

One of the important fields in nanotechnology research is the design of II–VI wide gap semiconductor composite structures to obtain novel properties for a variety of applications such as photonic devices, biological labeling, light-emitting diodes, and solar cells.^{1–3} The most studied systems are the nanocrystals of CdSe and ZnSe, their core/shell structures or $\text{Zn}_x\text{Cd}_{1-x}\text{Se}$ solid-solution nanocrystals and quantum dots.^{4–6} It is important for the mixed nanocrystals to exhibit a wide tunable absorption spectra, high luminescence efficiency, and the ability to tune the emission characteristics by varying the size, shape, and inherent composition. However, the applicability of the luminescent nanocrystals, such as stability and high luminescent quantum efficiency under real operation conditions, suffer from the passivation of dangling bonds present on the nanocrystal surface.⁷ To solve this problem, organic ligands were attached to the nanocrystal surface, which allowed high photoluminescence (PL) efficiency, but the PL efficiency was strongly dependent on the nanocrystal surroundings, due to oxidation of the particle surface.^{8,9} The nanocrystals were also encapsulated with silica to make them hydrophilic for biological applications, but involved the use of toxic reactants such as tetraethyl orthosilicate (TEOS).¹⁰ Recently, nanocrystals of diluted magnetic semiconductors were encapsulated with a carbon shell in order to reduce their toxicity for biological applications.^{11,12} Moreover, carbon encapsulation of the semiconductor nanocrystals have shown to improve the opti-

ABSTRACT $\text{Zn}_x\text{Cd}_{1-x}\text{Se}/\text{C}$ core/shell nanocrystals with 31–39 nm semiconducting core and 11–25 nm carbon shell were synthesized from solid state precursors in large scale amounts. A mixture of spherical and tripod nanostructures were obtained only in the one-step reaction (ZC3), where the Zn- and Cd-precursors were reacted simultaneously, rather than in the two step reactions (ZC1 and ZC2), where largely spherical nanostructures were observed. Rietveld analysis of the X-ray diffraction patterns of the samples prepared in three different ways, all under their autogenic pressure, reveal varying compositions of the $\text{Zn}_x\text{Cd}_{1-x}\text{Se}$ nanocrystal core, where the cubic phases with higher Zn content were dominant compared to the hexagonal phases. Carbon encapsulation offers excellent protection to the nanocrystal core and is an added advantage for biological applications. Cathodoluminescence (CL) measurements with spatially integrated and highly localized excitations show distinct peaks and sharp lines at various wavelengths, representing emissions from single nanostructures possessing different compositions, phases, and sizes. Transmission electron microscopy (TEM) showed striations in the nanocrystals that are indicative of a composition modulation, and possibly reveal a phase separation and spinodal decomposition within the nanocrystals. Thermal quenching of the luminescence for both the near band-edge and defect related emissions were observed in the range 60–300 K. The measured activation energies of ~50–70 meV were related to the presence of shallow donors or acceptors, deep level emissions, and thermal activation and quenching of the luminescence due to the thermal release of electrons from shallow donors to the conduction band or a thermal release of holes from shallow acceptors to the valence band. Spatially integrated CL spectra revealed the existence of broadening and additional components that are consistent with the presence of a composition modulation in the nanocrystals. Spatial localization of the emission in isolated single nanocrystals was studied using monochromatic CL imaging and local CL spectroscopy. CL spectra acquired by a highly localized excitation of individual nanocrystals showed energy shifts in the excitonic luminescence that are consistent with a phase separation into Zn- and Cd-rich regions. The simultaneous appearance of both structural and compositional phase separation for the synthesis of $\text{Zn}_x\text{Cd}_{1-x}\text{Se}$ nanocrystals reveals the complexity and uniqueness of these results.

KEYWORDS: $\text{Zn}_x\text{Cd}_{1-x}\text{Se}$ · nanocrystal · core–shell · XRD-Rietveld · cathodoluminescence · phase separation

cal properties and enhance the PL emission.^{13,14}

The ternary Zn–Cd–Se system in the form of nanowires,¹⁵ nanorods,¹⁶ nanocrystals,⁶ or quantum dots,¹⁷ and the core/shell ZnSe/CdSe counterparts^{18,19} were studied in great detail in the literature. The nanostructures were synthesized by a variety of techniques such as wet chemical synthesis which involve colloidal solutions,¹⁶ cation exchange reactions,²⁰ and capping of the

*Address correspondence to gedanken@mail.biu.ac.il.

Received for review February 10, 2009 and accepted June 15, 2009.

10.1021/nn9005076 CCC: \$40.75

© XXXX American Chemical Society

nanocrystals,² electrochemical deposition,²¹ metal-organic chemical vapor deposition,¹⁵ and molecular beam epitaxy.²² To meet technological demands for large scale synthesis, Kim *et al.* reported subkilogram-scale one-pot synthesis of the quantum dots, which involved the use of organic surfactants and solvents.¹ In the current study, the $\text{Zn}_x\text{Cd}_{1-x}\text{Se}/\text{C}$ nanocrystals were synthesized in sealed reactors, without the use of solvents and organic chemicals. We used 5 mL reactors in each batch of synthesis and obtained 0.6–0.8 g of the products. Because of the ease of this method, the product yield can be linearly scaled up to the kilogram scale simply by increasing the size of the reactor to fit in larger quantity of the reactants. Three different compounds were synthesized by changing the chronological order of reactants, to obtain varying $\text{Zn}_x\text{Cd}_{1-x}\text{Se}$ phases in the products. The product compositions and the percentage of each phase were found to be reproducible in three batches of samples. XRD revealed that the nanostructures crystallized in a two-phase mixture, involving both hexagonal and cubic phases, the latter being dominant. A protective carbon shell over the nanocrystal core was formed *in situ* within the reactor, without the use of any surfactant or carbon containing feed-stock gas.

Phase separation within ternary II–VI crystals is a rare phenomenon since growth temperatures are ordinarily greater than critical temperatures for the miscibility gap in the phase diagram.^{23,24} Nonetheless, spinodal decomposition in II–VI crystals has been predicted from thermodynamic considerations and observed.²⁵ Using high-resolution TEM, a spinodal-like phase separation was observed for $\text{Cd}_x\text{Zn}_{1-x}\text{Te}$ layers grown on GaAs substrates.²⁶ $\text{Zn}_{1-x}\text{Cd}_x\text{O}$ films grown on c-plane sapphire exhibited a substantial phase separation into Cd-rich and Zn-rich domains that were probed by cathodoluminescence (CL) wavelength imaging.²⁷ Of particular relevance is a study of phase separation for $\text{Zn}_x\text{Cd}_{1-x}\text{Se}$ epilayers grown on InP using organometallic vapor phase epitaxy which exhibited various mixed chemical phases having compositions, x , ranging from 0 to 1, as studied by CL and XRD.²⁸ In our present study of $\text{Zn}_x\text{Cd}_{1-x}\text{Se}$ nanocrystals, TEM showed striations in the nanocrystals that are indicative of a composition modulation, and possibly reveal a phase separation and spinodal decomposition.

To examine the relationship between the structural properties and the local optical properties we have used a combination of X-ray diffraction (XRD) and spatially and spectrally resolved CL. In particular, we attempt to correlate changes in the Zn cation alloy composition, x , with changes in the near-band-edge (NBE) luminescence associated with the nanocrystals on a submicrometer-size scale. We have employed the high-spatial resolution of CL, with its concomitant ability to scan the exciting high-energy electron beam, to analyze the influence of local changes in both composition x

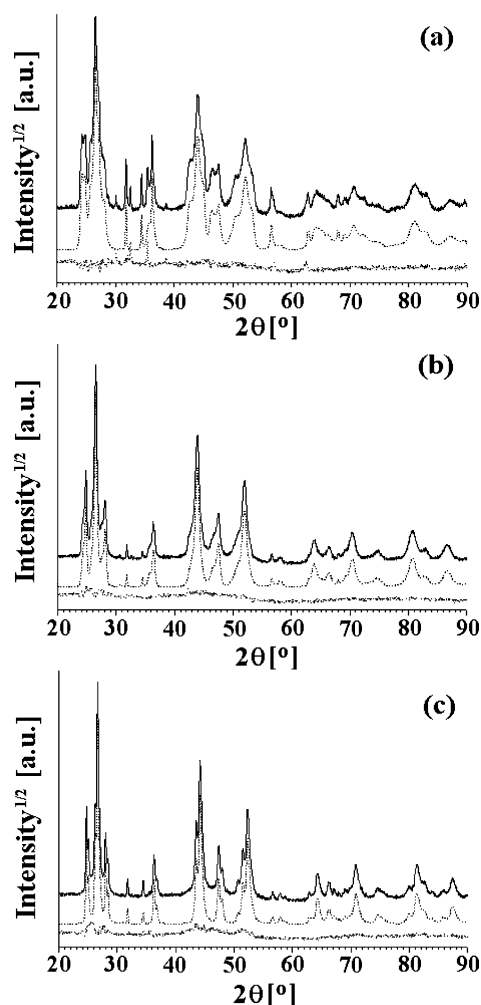


Figure 1. Weighted observed (solid), calculated (dashed), and difference (dotted) X-ray powder patterns of samples (a) ZC1, (b) ZC2, and (c) ZC3, after DDM refinement.

and phase on the emission wavelengths of the $\text{Zn}_x\text{Cd}_{1-x}\text{Se}$ nanocrystals. CL enables a highly localized excitation of the nanocrystals, and the resulting spectra reveal narrow emission lines with high luminescence efficiency. Likewise, monochromatic CL imaging reveals emission from sharply localized regions, as limited in size by the CL spatial resolution of $\sim 0.3\ \mu\text{m}$, that are indicative of emission from individual nanocrystals. We demonstrate that for each set of samples, high-quality $\text{Zn}_x\text{Cd}_{1-x}\text{Se}$ nanocrystals were formed during the growth process, yielding corresponding emission spectra in CL that are attributed to well-defined compositions and phases that correlate with local variations in the near-band edge excitonic emission energies. Additional features of the NBE emission were found to be blue- and red-shifted in energy relative to energy values expected for $\text{Zn}_x\text{Cd}_{1-x}\text{Se}$ nanocrystals possessing the identified set of compositions and phases measured with XRD. Such shifts are shown to be consistent with presence of a composition modulation and phase separation into Zn- and Cd-rich regions, as observed in the TEM

TABLE 1. Phase Composition of the Samples. The Parentheses in the Percentage Column Indicate the Standard Deviations of Phase Composition from Three Batches of Samples

sample	phase	composition		
		lattice	lattice parameter	percentage (%)
ZC1	(Zn _{0.93} Cd _{0.07})Se	cubic	$a = 5.701(1) \text{ \AA}$	27.5(3)
	(Zn _{0.66} Cd _{0.34})Se	cubic	$a = 5.8145(2) \text{ \AA}$	16.5(2)
	(Zn _{0.17} Cd _{0.83})Se	hexagonal	$a = 4.246(1) \text{ \AA}$, $b = 6.947(1) \text{ \AA}$	19.7(2)
	(Zn _{0.53} Cd _{0.47})Se	hexagonal	$a = 4.1439(8) \text{ \AA}$, $b = 6.788(1) \text{ \AA}$	7.9(3)
ZC2	(Zn _{0.61} Cd _{0.39})Se	cubic	$a = 5.8351(1) \text{ \AA}$	46.4(1)
	(Zn _{0.52} Cd _{0.48})Se	hexagonal	$a = 4.1499(3) \text{ \AA}$, $b = 6.7953(2) \text{ \AA}$	18.2(4)
	(Zn _{0.27} Cd _{0.73})Se	hexagonal	$a = 4.2196(3) \text{ \AA}$, $b = 6.9099(3) \text{ \AA}$	10.5(3)
ZC3	(Zn _{0.69} Cd _{0.31})Se	cubic	$a = 5.8010(2) \text{ \AA}$	41.5(2)
	(Zn _{0.50} Cd _{0.50})Se	cubic	$a = 5.878(1) \text{ \AA}$	7.3(1)
	(Zn _{0.47} Cd _{0.53})Se	hexagonal	$a = 4.1614(2) \text{ \AA}$, $b = 6.8079(2) \text{ \AA}$	14.5(2)
	(Zn _{0.66} Cd _{0.34})Se	hexagonal	$a = 4.107(1) \text{ \AA}$, $b = 6.727(1) \text{ \AA}$	9.4(1)

images. An analysis of the interplay between composition, phase, and size is presented in a thorough discussion of the spectrally and spatially resolved CL results.

RESULTS AND DISCUSSION

The composition of the final products was examined with inductively coupled plasma (ICP) and Rietveld refinement of the powder X-ray diffraction (XRD) patterns. ICP analysis showed the composition of the solid products according to the Zn: Cd atomic ratio of 1.85, 1.2, and 1.18, and are designated as ZC1, ZC2, and ZC3, respectively, throughout the paper. The atomic ratios of Se: Zn were 1.12, 1.58, and 1.6 for ZC1, ZC2, and ZC3, respectively. The full-profile analysis of the XRD patterns was done by applying the Rietveld formalism²⁹ and the derivative difference minimization (DDM)³⁰ refinement method. The final agreement between the observed and calculated XRD profiles is illustrated by Figure 1. The crystalline fraction (ca. 75 wt %) of the samples was modeled by a mixture of cubic and hexagonal Zn/ Cd selenides (Table 1). NaF powder was used as an internal standard for the crystalline weight percent assessment. The Zn/ Cd ratios in the structures were estimated on the basis of the specific volumes per structural unit derived from the refined lattice parameters. The reference specific volumes for pure ZnSe (45.5 Å³) and CdSe (56.1 Å³) were calculated using the lattice constants available from the ICDD PDF database entries 37–1463 and 8–0459.

Figure 2a–e illustrates the high resolution scanning electron microscope (HRSEM) images of the nanocrystals. As is evident from the images, all the three products are composed of core–shell morphology. The

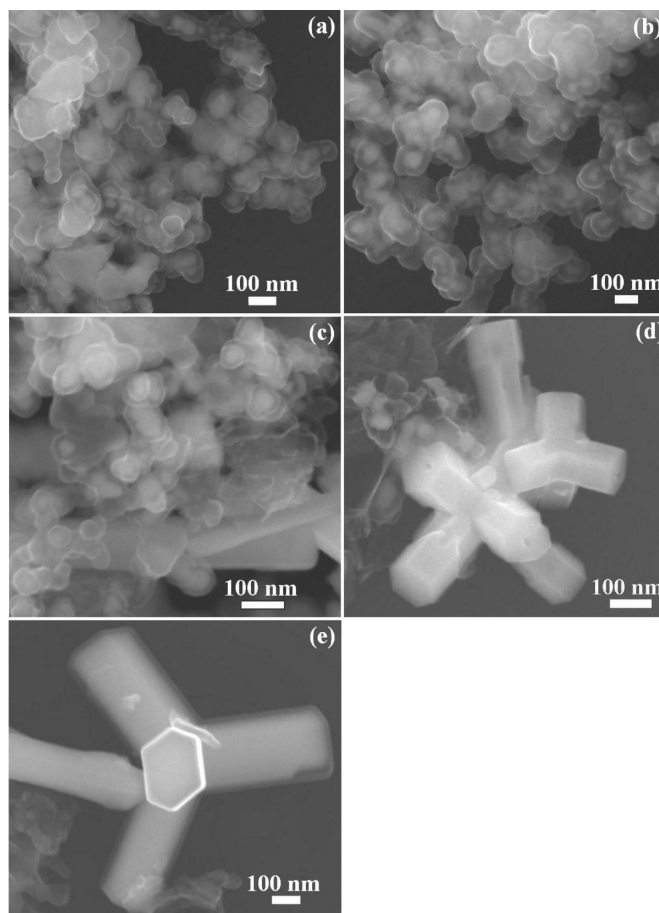


Figure 2. HRSEM images: (a) ZC1, (b) ZC2, (c) ZC3, (d) tripods in ZC3, and (e) hexagonal face of a tripod in ZC3.

shell is composed of carbon and the carbon content determined from C, H, N analysis is 2.6, 3.9, and 2.9 wt % in ZC1, ZC2, and ZC3 products, respectively. The nanocrystals in ZC1 and ZC2 are primarily spherical in shape, the core being 31 ± 14 and 36 ± 9 nm, and the shell is 18 ± 3 and 25 ± 2 nm, respectively. In ZC3, a mixture of spherical and tripod nanostructures are observed. The spherical nanocrystals of ZC3 have 30 ± 3 nm core surrounded by 11 ± 2 nm shell. The tripods are larger in dimensions with the branching length between 100 to 475 nm. A representative hexagonal face of a branch is shown in Figure 2e. The edges of the hexagon are ~ 126 nm and the distance between the edges is ~ 200 nm. The core of the tripods is surrounded by a ~ 16 nm carbon shell. When the nanocrystals were synthesized at 1000 °C, the size of the nanocrystals increased, keeping the phase compositions intact to those synthesized at 800 °C. However, all the samples are highly polydisperse, especially in comparison to standards typical for colloidal syntheses.

The TEM images in Figure 3 reflect the results from the SEM micrographs. ZC1 consists of ellipsoidal to spherical nanocrystals, the dimensions of the core are ~ 62 and ~ 37 nm length and breadth wise, respectively. Several hollow carbon shells are observed with

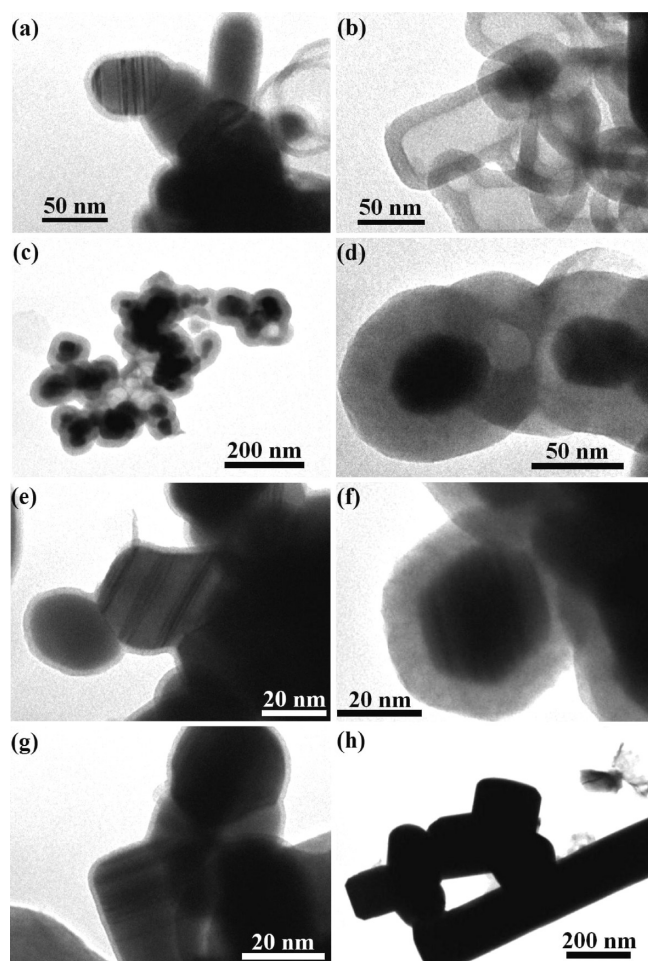


Figure 3. Bright field TEM images: (a) ZC1, (b) hollow carbon shells in ZC1, (c) ZC2, (d) magnified view of a core/shell structure of a nanocrystal in ZC2, (e) striations within the nanocrystal in ZC2, (f) core/shell structure of a nanocrystal in ZC3, (g) striations, and (h) tripods in ZC3.

a core of ~ 29 nm and shell of ~ 11 nm. In ZC2, the core and shell are ~ 39 and $21\text{--}25$ nm, respectively. Figure 3d illustrates an enlarged view of the core ($\sim 38 \pm 2$ nm)/shell ($\sim 24 \pm 2$ nm). A single nanostructure of ZC3 is shown in Figure 3f, where the hexagonal ~ 31 nm core is shielded by a ~ 8 nm shell. Significant striations are observed in the nanocrystals of ZC1 (Figure 3a), ZC2 (Figure 3e), and ZC3 (Figure 3f and 3g). These striations indicate a composition modulation and spinodal decomposition within the nanocrystals (also evident from CL studies).

X-ray dot mapping of a selected area of ZC1 shows a uniform distribution of Zn, Cd, Se, and C (Figure S1). The results obtained from energy dispersive X-ray spectroscopy (EDS) coupled with HRSEM are shown in Figure 4. The dispersion of the sample in dry ethanol was spread onto a silicon wafer and dried in a glovebox. The EDS spectra were recorded at five different locations. The Zn:Cd atomic ratios obtained from the EDS results are 1.7(3), 1.1(0), and 1.2(2) for ZC1, ZC2, and ZC3, respectively. These values match well with the quantitative analysis by ICP measurements. The forma-

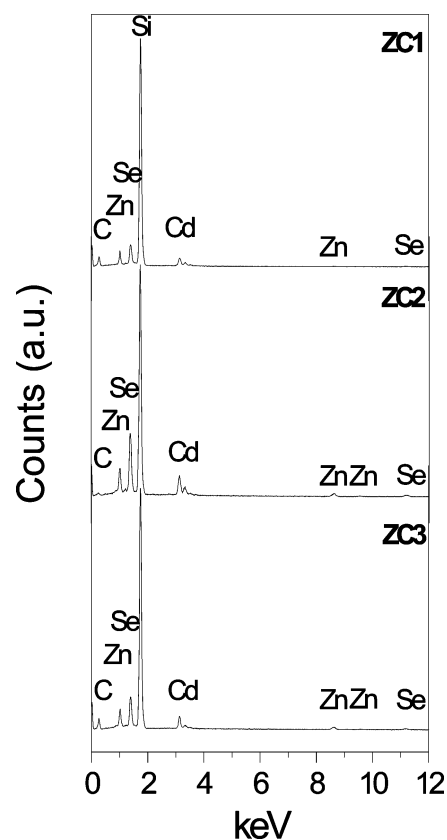


Figure 4. The EDS results of ZC1, ZC2, and ZC3.

tion mechanism of the carbon encapsulated nanocrystals has been discussed in detail.^{11,12} The formation of the carbon shell over the semiconducting core is a kinetically controlled process. The reactions occur in the gaseous phase after the respective acetates decompose at an elevated temperature to give the final products after solidification. It is worth mentioning here that the nanocrystals of ZC1 and ZC2 were synthesized by a two step process, wherein the initial ZnSe/C and CdSe/C nanocrystals react with the next reactants to form $\text{Zn}_x\text{Cd}_{1-x}\text{Se/C}$ products. At high temperatures (800°C), the carbon shell (of ZnSe/C and CdSe/C) exfoliates under autogenic pressure to allow the Cd- or Zn-acetates and Se to react with the nanocrystal core. Carbon forms the final shell over the nanocrystal since the solidification rate of the nanocrystal core is faster than carbon.^{11,12}

Temperature-Dependent Spatially Integrated CL Results. Because of the carbon shell encapsulating the nanocrystal core, the surface of the $\text{Zn}_x\text{Cd}_{1-x}\text{Se}$ nanocrystals are very well passivated, to the extent that continuous exposure to the electron beam did not result in diminished luminescence intensity. In Figure 5, we show spatially integrated CL spectra of the three samples in the wavelength range $450 \leq \lambda \leq 850$ nm for various temperatures ranging from 60 to 300 K. Emission was not detected in the $300 \leq \lambda \leq 450$ nm range for all three samples. As observed in the figure, the peak positions

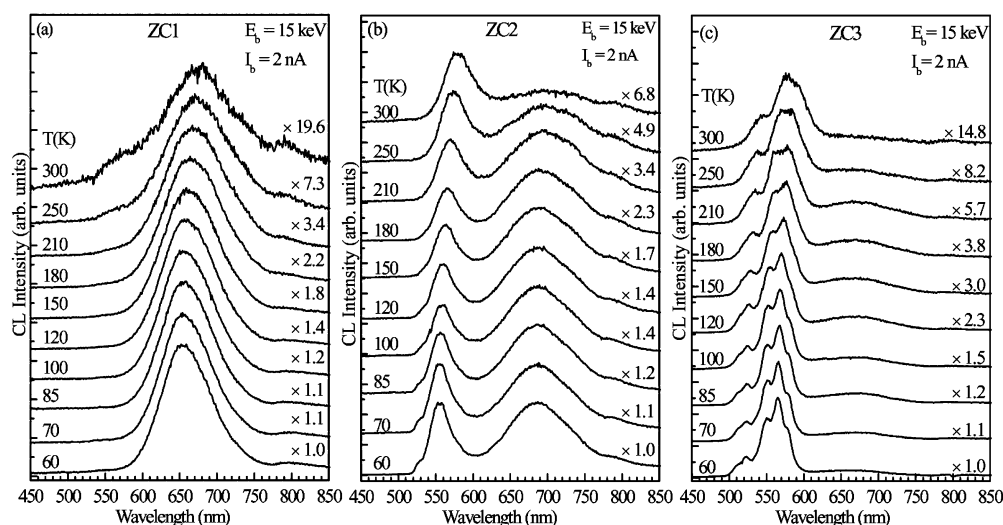


Figure 5. Spatially integrated CL spectra acquired at various temperatures from 60 to 300 K. The e-beam was rapidly rastered over a $64\ \mu\text{m} \times 48\ \mu\text{m}$ region of each sample during the measurements to yield spectra representative of the average emission for nanocrystals in each sample.

and line shape are markedly different for each of the spectra. For ZC2 and ZC3, broad emissions centered about $\sim 560\ \text{nm}$ (2.214 eV) are observed, exhibiting multiple components that represent near band-edge (NBE) excitonic emission from the various $\text{Zn}_x\text{Cd}_{1-x}\text{Se/C}$ nanocrystals possessing different compositions and phases. These emissions are largely absent in ZC1 and only a broad deep-level (DL) emission from 590–750 nm centered at $\sim 655\ \text{nm}$ (1.893 eV) is observed. As we shall discuss later, NBE emission features in ZC1 were observed in the local CL spectroscopy measurements. Such a DL emission type has previously been observed in various ZnSe films and nanocrystals and has been attributed to various mechanisms involving structural and point defects.^{31–35} The presence of cation vacancies and Se interstitials gives rise to acceptor states, while Se vacancies and cation interstitials produce donor states.^{36,37} Thus, the DL emission has been attributed to a donor–acceptor pair (DAP) radiative recombination.^{31,36,37} Recent experiments involving the annealing of as-grown ZnSe nanowires in a Zn-rich atmosphere confirm that the two species involved in the DAP are Zn vacancies and Zn interstitials.³⁷ The situation is of course more complex for $\text{Zn}_x\text{Cd}_{1-x}\text{Se}$ alloys, since Cd vacancies and Cd interstitials could also contribute to the acceptor and donor states, respectively, and make a precise identification of the cation and anion species involved in DAP transitions more difficult. Nonetheless, as a result of the similarity with the broad DL emissions observed in ZnSe nanowires,^{36,37} we also attribute the broad emissions in our $\text{Zn}_x\text{Cd}_{1-x}\text{Se/C}$ alloys from ~ 590 to 750 nm (2.10 to 1.65 eV) to radiative recombination involving DAP transitions, as observed in Figure 5. In our present study, we observe intense DL emissions in ZC1 and ZC2, and a reduced DL emission intensity in ZC3. Additional smaller peaks are observed

toward larger wavelengths (just below the PMT cutoff of $\sim 850\ \text{nm}$) in the three samples and again represent additional DL transitions ascribed to various point and structural defects.

Determination of the Activation Energies for the Thermal Quenching of the Luminescence. We have examined the temperature dependence of the CL spectra for the three samples in the range $60 \leq T \leq 300\ \text{K}$. Scale factors for the CL spectra are indicated on the right of each spectrum in Figure 5. For ZC2 and ZC3, the CL peaks associated with the NBE excitonic emission decrease in intensity as the temperature is increased over the full range, but the line shape of the spectra including the positions of the shoulders and other features of the spectra remain relatively unchanged except for the apparent broadening at higher temperatures ($T > \sim 180\ \text{K}$). A similar decrease in the DL emission for all samples is also observed as the temperature is increased over the range of $60 \leq T \leq 300\ \text{K}$. The CL peak energies of the major features for each of the samples in Figure 5, including the central peak position of the DL related features, exhibit a red shift of $\sim 80\ \text{meV}$ as the temperature is raised from 60 to 300 K. This is essentially consistent with the expected temperature dependence of the bandgap for $\text{Zn}_x\text{Cd}_{1-x}\text{Se}$ in both the cubic and hexagonal phases when comparing with the temperature dependence of the bandgap for pure ZnSe and CdSe crystals.³⁸ To further analyze the thermal activation behavior, the temperature dependence of the various peak intensities, I , were fitted to a standard model for the thermal quenching of the luminescence. The model involves a thermal activation energy, E_A , as $I = I_0[1 + \alpha \exp(-E_A/k_B T)]^{-1}$, where I_0 and α are additional fitting parameters that depend on the maximum intensity at low temperature and the intermediate temperature below which the intensity curve begins to saturate.³⁹ The

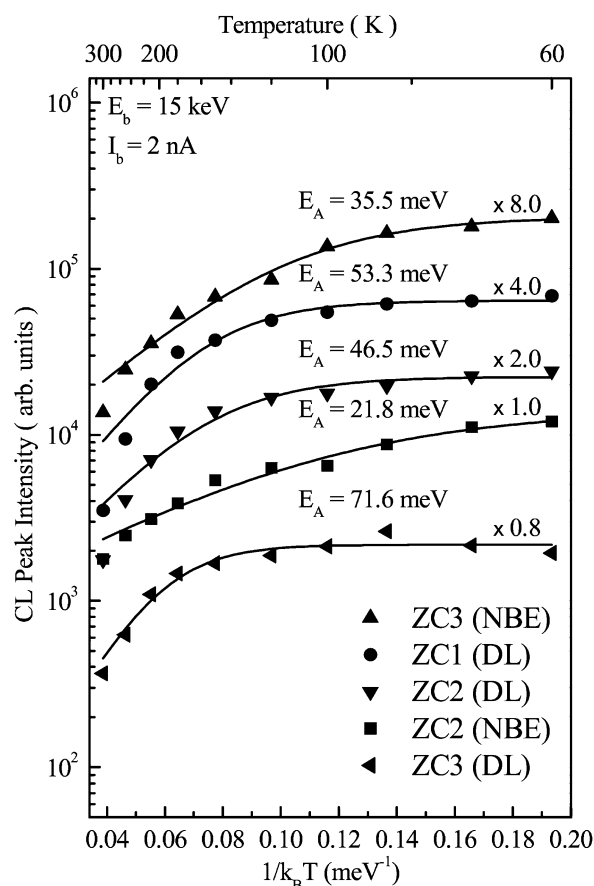


Figure 6. CL peak intensities as a function of $1/k_B T$. The temperatures are read more clearly from the upper abscissa. Using the general fitting formula for thermal quenching of luminescence in semiconductors, $I = I_0[1 + \alpha \exp(-E_A/k_B T)]^{-1}$, activation energies (E_A) were extracted and shown above each fitting curve for the three samples. Fits were performed for the observable near band emission (NBE) peaks as well as for the deep level (DL) emission features.

results of the fits are shown with the solid curves running through the data points in Figure 6, which are denoted with the various symbols indicating the appropriate peaks for each of the three samples. The results of the fits for the NBE peaks of ZC2 and ZC3 yield activation energies of 21.8 ± 3.4 and 35.5 ± 3.2 meV, respectively. For the broad DL emission peaks, activation energies of 53.3 ± 8.7 , 46.5 ± 9.1 , and 71.6 ± 19.7 meV are obtained for ZC1, ZC2, and ZC3, respectively.

The maximum CL luminescence efficiency at $T = 60$ K was determined by fixing the e -beam injection at a single location for samples ZC2 and ZC3 and acquiring locally CL spectra at various points on the samples. The integrated CL emission for the NBE peaks at each point was compared with the integrated CL intensity for a reference InGaN/GaN multiple quantum well sample of known CL luminescence efficiency, acquired under the same excitation conditions ($E_b = 15$ keV and $I_b = 100$ pA) and temperature.⁴⁰ Such a comparison, which took into account the wavelength-dependent response of the optical detection system, resulted in maximum CL efficiencies of $\sim 45\%$ and $\sim 35\%$ for samples ZC2 and

ZC3, respectively, at $T = 60$ K, for local excitation. The average decrease in CL efficiency with temperature is similarly represented by the temperature dependence of the CL intensity in Figure 7, indicating a reduction in average CL efficiency by factors of 6.8 and 14.5 for ZC2 and ZC3, respectively, over the temperature range of $60 \leq T \leq 300$ K.

We attribute the thermally activated behavior of the NBE peaks as due to the usual presence of point defects, impurities, and a possible absence of a complete surface passivation for the nanocrystals, all of which contribute to activated barriers associated with the nonradiative recombination as the temperature increases. The measurably lower E_A for ZC2 in comparison to that for the NBE peak of ZC3 may also relate to the substantially larger contribution of the DL emission in the former sample. In particular, the larger rate of defect and impurity related recombination (as exhibited in the larger DL emission) in ZC2 also appears to be reflected in the lower activation energy of the NBE peak (21.8 meV) associated with carriers reaching these channels. Consequently, the reduced DL emission in ZC3 correlates well with the higher activation energy (35.5 meV) for the NBE emission, suggesting that accessing the defect/impurity channels require a greater thermal energy in this sample in comparison to that for ZC2. An absence of a measurable NBE feature in ZC1 for the spatially integrated CL spectrum of Figure 5 prevented such an analysis. The extracted activation energies for the DL features for all samples reflect most likely the positions of shallow donors or acceptors in the $\text{Zn}_x\text{Cd}_{1-x}\text{Se}$ band gap. For ZnSe, the deep-level donor associated with isolated Zn^{2+} interstitials is located ~ 0.9 eV below the conduction band minimum and the deep-level acceptor vacancy $\text{V}_{\text{Zn}}^{2-}$ is ~ 0.7 eV above the valence band maximum for DAP pairs whose interstitial-vacancy ($\text{Zn}_i^{2+} - \text{V}_{\text{Zn}}^{2-}$) separations are infinite.^{31,32} As the $\text{Zn}_i^{2+} - \text{V}_{\text{Zn}}^{2-}$ separation is reduced, the Coulomb interaction energy will lead to higher energy DAP transition energies and contribute to the broadened DL emission that is observed.^{31,32,36,37} For the present $\text{Zn}_x\text{Cd}_{1-x}\text{Se/C}$ samples, we would likewise expect doubly charged ($n = 2$) interstitials and vacancies to contribute deep levels several hundreds of meV within the bandgap. Thus, we attribute the measured activation energies of ~ 50 – 70 meV to reflect the presence of shallow donors or acceptors that are involved in the DL emission for which thermal activation and quenching of the luminescence is attributed to a thermal release of electrons from shallow donors to the conduction band or a thermal release of holes from shallow acceptors to the valence band. The DAP transitions likely involve, to some degree one donor or acceptor that is deep ($n = 2$) since the DL emission energy is 0.35–0.45 eV below the NBE peaks (Figure 5). However, given the more complex situation of the $\text{Zn}_x\text{Cd}_{1-x}\text{Se}$ alloy with both hexagonal and cubic phases, we can only hypothesize that

the shallow impurity levels that contribute to the DL emission involve charged interstitial and vacancy states (Zn^{n+} , Cd^{n+} , $\text{V}_{\text{Zn}}^{2-}$, $\text{V}_{\text{Cd}}^{2-}$) that possess charges represented by $n \leq 1$.^{31,32}

Decomposition of the Spatially Integrated CL Spectra into Distinct Gaussian Components Using a Nonlinear Least-Squares Fitting Procedure. A closer inspection of Figure 5 shows that the spatially integrated CL spectra for ZC2 and ZC3 exhibit distinct peaks and shoulders in the NBE part of the spectrum from $\sim 500 \text{ nm} \leq \lambda \leq 600 \text{ nm}$. Given the discrete set of compositions, x , for the various $\text{Zn}_x\text{Cd}_{1-x}\text{Se}$ nanocrystals that were obtained in the XRD results, we hypothesize that each feature (*i.e.*, a broad peak or shoulder) in the NBE emission corresponds to distinct emissions from groups of nanocrystals that possess the same discrete values of x . To test this hypothesis, we have decomposed the spatially integrated CL spectra (with abscissa now represented in energy) for ZC2 and ZC3 at 60 K into a sum of discrete Gaussian peaks, as shown in Figure 7, using a nonlinear least-squares fitting procedure in OriginPro v. 8.0. A minimum number of Gaussian components for each CL spectrum were used such that each component should actually correspond to a peak or distinct shoulder in the original data. The resulting fits are indicated by the dotted lines running through the experimental data with the individual Gaussian components offset below the data and fit for clarity. For each spectrum, we have labeled the fits with components P_i ($i = 1-5$ or 6) with the corresponding wavelength equivalent of the peak position shown in the key.

The peak P1 in each spectrum corresponds to the DL emission. The remaining peaks in the NBE peaks correspond to emissions from the various $\text{Zn}_x\text{Cd}_{1-x}\text{Se}/\text{C}$ nanocrystals. The energies of the decomposed components (P_i) were analyzed with an attempt to identify the phases and compositions of the particular nanocrystals from which the components are derived (from XRD-Rietveld analysis). The dependence of the energy gap for $\text{Zn}_x\text{Cd}_{1-x}\text{Se}$ deviates slightly from a pure linear interpolation between the ZnSe and CdSe gap energies (*i.e.*, E_{ZnSe} and E_{CdSe}), and such downward bowing is commonly found for thin film alloys of II–VI semiconductors.^{41,42} The nonlinear variation of the energy gap, $E_g(x)$, for $\text{Zn}_x\text{Cd}_{1-x}\text{Se}$ can be represented as

$$E_g(x) = E_{\text{CdSe}} + (E_{\text{ZnSe}} - E_{\text{CdSe}} - b)x + bx^2 \quad (1)$$

where x is the composition of Zn, E_{ZnSe} and E_{CdSe} are the energy gaps for the pure crystals, and b is the bowing parameter. The parameters E_{ZnSe} , E_{CdSe} , and b are in general temperature and phase dependent, as the difference in gap energies between II–VI crystals in the cubic and hexagonal phases are well-known.⁴³ Among the various reported bowing parameters for the ZnSe and CdSe in the cubic and hexagonal crystals, the recent consensus appears that $b_h = 0.45$ and $b_c = 0.30$ re-

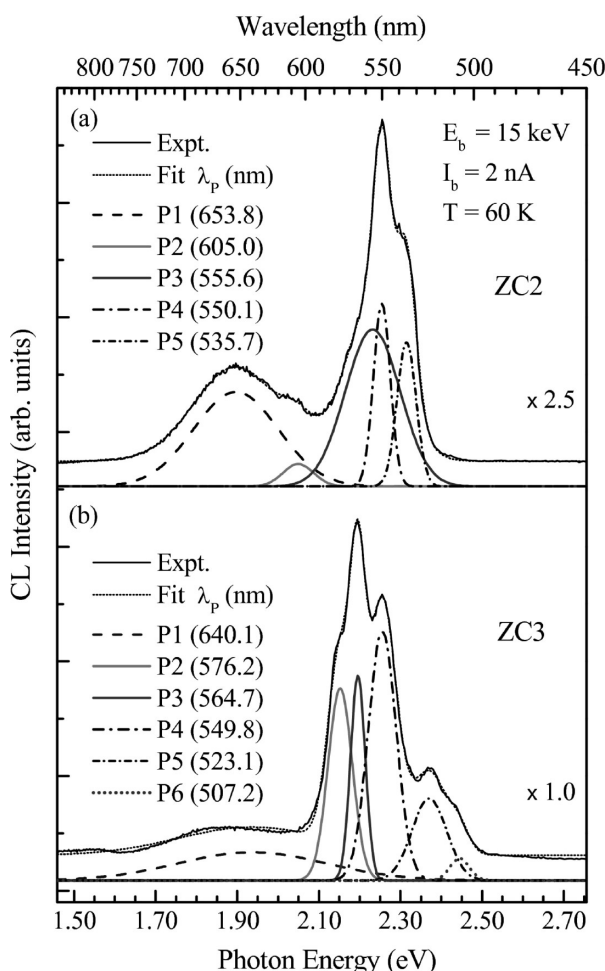


Figure 7. Spatially integrated CL spectra of the NBE for ZC2, and ZC3. Fits were performed in energy space whereas the peak positions are displayed as wavelengths. The experimental data, the resultant fit, and peaks P_i are indicated.

main good approximations independent of temperature, where the subscripts h and c denote the hexagonal and cubic phases, respectively.^{44–46} The bandgaps for ZnSe and CdSe in both the hexagonal and cubic phases at $T = 60 \text{ K}$ are approximated, respectively, as follows: $E_{\text{ZnSe}}^h = 2.86 \text{ eV}$ and $E_{\text{CdSe}}^h = 1.84 \text{ eV}$ (hexagonal); $E_{\text{ZnSe}}^c = 2.80 \text{ eV}$ and $E_{\text{CdSe}}^c = 1.75 \text{ eV}$ (cubic).³⁸ The resulting composition dependent bandgaps for the hexagonal and cubic phases are then expressed as follows:

$$E_g^h(x) = 1.84 + 0.57x + 0.45x^2 \quad (2)$$

$$E_g^c(x) = 1.75 + 0.75x + 0.30x^2 \quad (3)$$

With these expressions, it is now possible to determine the compositions (x) and phases (h or c) associated with the various components P_i in Figure 7. By comparing with the XRD results, the best match for the components P2, P3, P4, and P5 for the CL spectrum of ZC2 (Figure 7a) yields compositions and phases 0.298 (h), 0.494 (h), 0.517 (h), and 0.606 (c), respectively. These values agree well with the XRD results, that is, 0.27 (h),

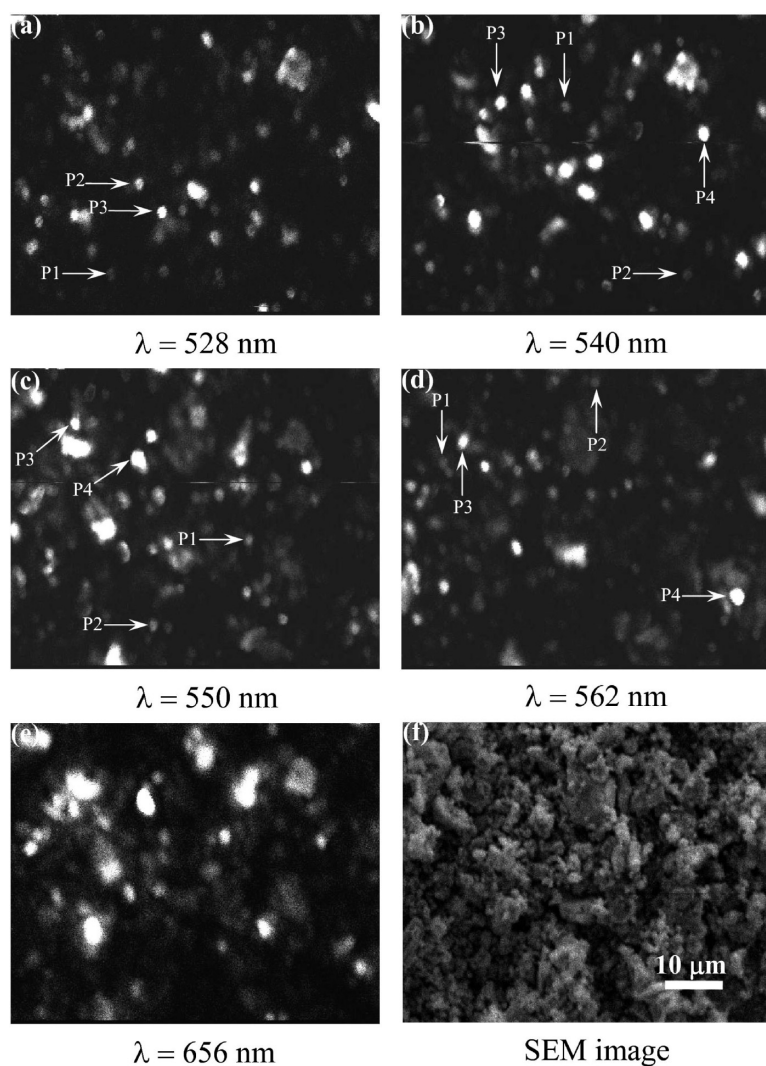


Figure 8. Monochromatic CL images for ZC2 at $T = 60$ K. Various wavelengths were chosen for the imaging, as indicated under each CL image in panels a–e. The SEM image of the corresponding region is shown in panel f. Various points P_i with arrows indicate points where local CL spectra were acquired.

0.52 (h), and 0.61 (c). The additional component P3 is actually ~ 3 times broader than the P4 component, and reflects the composition modulation, as evidenced by the striations in the TEM images (Figure 3e). The width of P3 is ~ 130 meV and would suggest a composition modulation of $0.494 \pm \sim 0.065$ (h). That is, a composition modulation of $\Delta x \approx 0.13$ is consistent with presence and width of peak P3 in Figure 7a.

For ZC3 (Figure 7b), peak P2 at $\lambda = 576.2$ nm represents a composition of 0.412 (h) or 0.453 (c), which appear to deviate significantly from the nearest XRD results of 0.47 (h) and 0.50 (c). However, peak P3 at $\lambda = 564.7$ nm represents emission from nanocrystals possessing compositions of 0.458 (h) and 0.496 (c), according to eqs 2 and 3, respectively. These are sufficiently close, within the experimental uncertainties, to the aforementioned XRD results. Thus we attribute the large peak P3 (564.7 nm) as due to a combination of emissions from nanocrystals possessing compositions

~ 0.47 (h) and ~ 0.50 (c). Continuing with peak P4 (549.8 nm), application of eqs 2 and 3 yields compositions of 0.517 (h) and 0.552 (c), again possessing a deviation too large for identification with any of the compositions and phases from XRD. However, a phase separation of crystalline material with ~ 0.465 (h) (that is, a spinodal decomposition of the material with hexagonal phase represented by P3) into regions of 0.41 (h) and 0.52 (h) would correlate precisely with the wavelength positions of P2 (576.2 nm) and P4 (549.8 nm). Again, the TEM images of Figure 3f,g exhibit striations, representing Zn-rich and Cd-rich regions, and support the notion of such a composition modulation. Thus, we hypothesize that a composition modulation of $\Delta x \approx 0.11$ in ZC3 is responsible for emissions in the CL spectrum of Figure 7b that are represented by the P2 and P4 components, which are positioned on opposite sides of the P3 peak.

In Figure 7b, peak P5 at 523.1 nm could correspond to compositions of 0.624 (h) and/or 0.655 (c), whereas peak P6 at 507.2 nm could represent emission from nanocrystals having compositions of 0.688 (h) and/or 0.719 (c). Since the XRD analysis yields 0.66 (h) and 0.69 (c), the deviation of ± 0.04 for each of the possibilities listed for peaks P5 and P6 would prevent an unambiguous identification. However, the XRD also shows a much greater composition of nanocrystals with 0.69 (c) in comparison to that for 0.66 (h), as the former shows a 41.5% composition in comparison to the latter which exhibited 9.4%. Since the ratio of the integrated intensities for peaks P5 and P6 is also ~ 4 , it is therefore likely and reasonable that P5 (523.1 nm) and P6 (507.2 nm) correspond to emissions from nanocrystals possessing compositions 0.69 (c) and 0.66 (h),

respectively. Thus, spectrally resolved CL together with XRD has enabled the identification of all major components of the spatially integrated CL spectra for the NBE associated with $\text{Zn}_x\text{Cd}_{1-x}\text{Se}$ nanocrystals possessing different compositions and phases. A phase separation that results in composition undulations of $\Delta x \approx 0.11$ to 0.13 is found to broaden and introduce additional components in the CL spectra of these samples.

Monochromatic CL Imaging and Acquisition of CL Spectra by Local Excitation with the e-Beam. To examine the spatial origins of the NBE emission from each of the samples, monochromatic CL images (as shown in Figure 8a–e) were acquired at $T = 60$ K at various wavelengths that are associated with the NBE features seen in the spatially integrated CL spectra of Figures 5 and 7. Figure 8f shows the SEM image of a region in ZC2 from which five monochromatic CL images were acquired. For the shorter wavelengths in the NBE region, it is clear that the monochromatic CL imaging reveals sharp highly lo-

calized emission features whose intensities vary from point to point. As the wavelengths approach the range for DL emission, as shown in Figure 8e, the size of the features appears to broaden, indicative of a more uniform distribution of DAP emission due mainly to larger spectral line width of the DL feature. By changing the wavelength in the NBE region ($528 \leq \lambda \leq 656$ nm) the spatial locations of the sharp bright dots in the monochromatic CL image rapidly change over this wavelength range. Thus, it is apparent that the bright dots represent emission from individual $\text{Zn}_x\text{Cd}_{1-x}\text{Se}$ nanocrystals whose compositions, phases, and sizes vary over the surface of the film. To further examine the local nature of the emission from these nanocrystals, we have acquired CL spectroscopy locally from selected regions at $T = 60$ K. For each of the four monochromatic CL regions in Figure 8a–d, three to four spots were arbitrarily selected whose intensities in the images vary from low to high, and as such are labeled P1–P4. At each point, a local CL spectrum was acquired with the electron beam fixed on the denoted spot. The local CL spectra for ZC2 are displayed in Figure 9a–d. Sharp peaks with strong emission intensities having minimum linewidths as narrow as ~ 15 meV are observed in Figure 9. Thus, the sharp CL lines are consistent with emission from the individual nanocrystals identified as bright dots in the CL images. Most of the sharp lines have peak wavelengths which fall approximately within the set of decomposed Gaussian peaks (P1–P5) that are presented in Figure 7a.

Variations in peak positions are again attributed to fluctuations in composition effects and yield peak positions outside the range of the decomposed peaks in Figure 7. For example, the sharp features at 527.6 and 530.6 nm in Figure 9a are blue-shifted by 36 and 22 meV, respectively, relative to the P5 (535.7 nm) component in Figure 7a, possibly owing to composition variations. Application of eq 3 yields compositions of 0.638 (c) and 0.626 (c), respectively, for these features which conceivably could reflect measurable compositional fluctuations above the value of 0.61 (c) obtained by XRD. Similarly, a group of peaks centered about ~ 540 nm are observed in Figure 9b. Acquisition of these local CL spectra were motivated by the spots of varying CL intensity observed in the monochromatic ($\lambda = 540$ nm) image of Figure 8b. Application of eq 2 yields $x = 0.556$ (h), which represents a composition change of ~ 0.04 relative to that represented by the P4 peak ($\lambda = 550.1$ nm) of Figure 7a. Such a large fluctuation is consistent with the maximum changes of $\Delta x \approx 0.11$ – 0.13 that were analyzed from the components of Figure 7. The remaining sharp peaks in Figure 9c,d correspond well with peaks P3 (555.6 nm) and P4 (550.1 nm) displayed in Figure 7a.

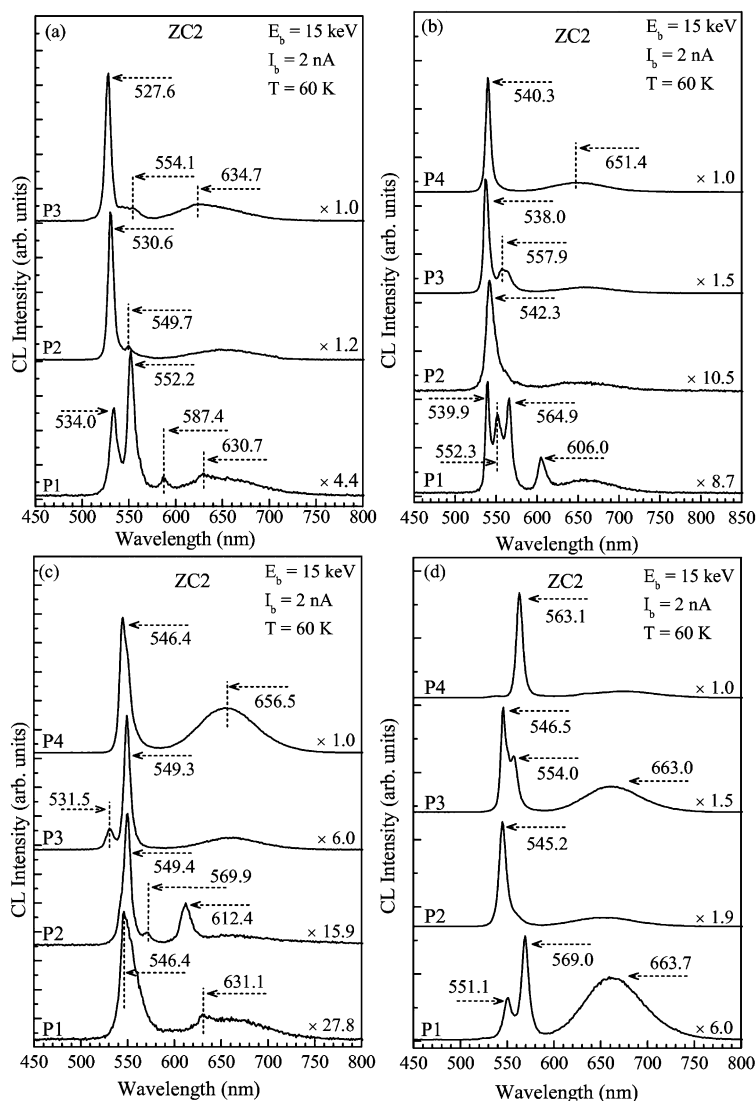


Figure 9. Local CL spectra for ZC2 at $T = 60$ K. The spectra were acquired by a focused e -beam excitation at the various points P_i shown in the monochromatic CL images of Figure 8. Each spectrum labeled as P_i in the panels a–d refer to the spots (also appropriately labeled with P_i) in the corresponding panels a–d of Figure 8. Peak positions in units of nm are indicated for the major peaks with the use of dashed arrows. Relative scale factors for each of the spectra are shown.

Monochromatic CL images involving wavelengths related to the DL emission (594–686 nm) for ZC1 are shown in Figure 10. Again random spots, a few with spot sizes smaller than ~ 0.5 μm , are clearly observed and indicative of emission from single nanocrystals. The local CL spectra of Figure 11a–c correspond one-to-one with the monochromatic CL images of Figure 10a–c for ZC1. However, unlike in the spatially integrated CL spectra of Figures 5 and 7 for ZC1, the local CL spectra in Figure 11 reveal the presence of sharp NBE emission features, although still considerably weaker than that observed for the other two samples. Such a local excitation with a highly focused e -beam leads to a greater chance that isolated nanocrystals possessing a higher than average luminescence efficiency for the NBE emission will be excited, emit luminescence, and

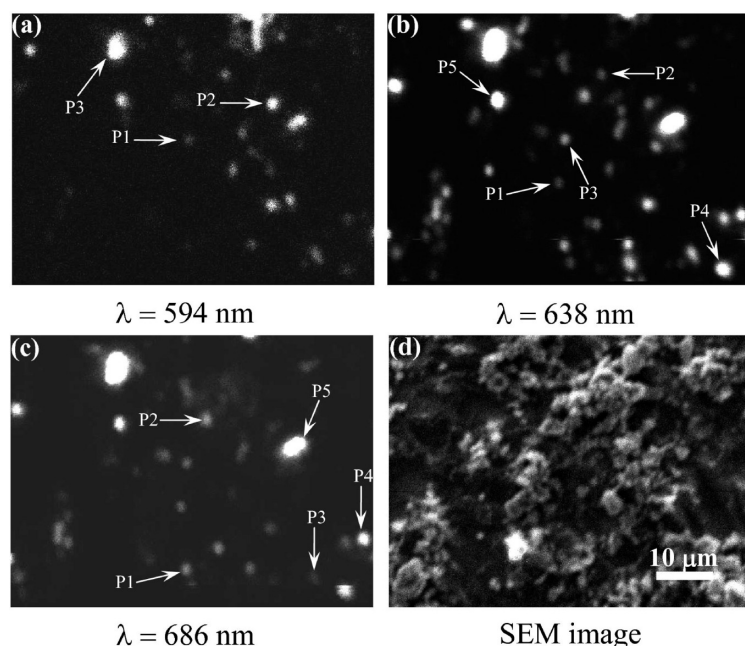


Figure 10. Monochromatic CL images for the ZC1 at $T = 60$ K. Various wavelengths were chosen for the imaging, as indicated under each CL image in (a)–(c). The SEM image of the corresponding region is shown in (d). Various points P_i with arrows indicate points where local CL spectra were acquired.

thus be detected. In contrast to the spatially integrated CL spectra for ZC1 in Figure 5, identification of the NBE peaks in the local CL spectra allows for an analysis of the nanocrystal compositions. Peaks at 509.4 and 510.4 nm in Figure 11a,c, respectively, correspond to $x \approx 0.708$ (c) using eq 3. While this is not very far from the $x = 0.66$ (c) value obtained in XRD, the deviation of $\Delta x \approx 0.05$ also suggests that compositional variations are responsible since eq 3 predicts $\lambda \approx 522$ nm for $x = 0.66$ (c). Several sharp peaks in Figure 11b,c are observed to

be in the range of $\sim 530 \leq \lambda \leq 541$ nm. The next expected composition is 0.53 (h) from XRD which corresponds to $\lambda \approx 546$ nm from eq 2. Again, we hypothesize that compositional fluctuations of $\Delta x \approx 0.02$ – 0.07 cause a ~ 20 to 70 meV blue-shift relative to the predicted peak energy. Another salient aspect, the local CL spectrum of Figure 11 is that the position of the DL emission feature appears roughly tied to the position of the NBE peak for each spectrum. An energy difference of ~ 400 meV is observed between these features in most of the spectra where the NBE can be unambiguously identified as emission within a single peak. This observation is also consistent with the local emission being derived from single $\text{Zn}_x\text{Cd}_{1-x}\text{Se}$ nanocrystals since, as previously discussed, the defect levels are directly tied to the band edges and thus the band gap shifts associated with compositional changes will result in corresponding shifts in the DAP transition energies. Fluctuations in the large energy difference between the NBE and DL features (~ 0.4 eV) can also be attributed fully or partially to composition fluctuations.

The monochromatic CL images and local CL spectra for ZC3 are very similar to those of ZC2.

For ZC3, the monochromatic CL images in the 504–571 nm range again exhibited small bright spots ranging from ~ 0.3 to ~ 5 μm in size, and limited by the spatial resolution of the CL technique (Figure S2). The density of the bright spots was wavelength dependent, and a sharp drop in dot density was observed when $\lambda = 504$ nm and is close to the high-energy limit for NBE. Similar fluctuations of the emission energies in ZC3 were observed (Figure S3). For each monochromatic imaging wavelength of ZC3, sets of distinct bright spots in the

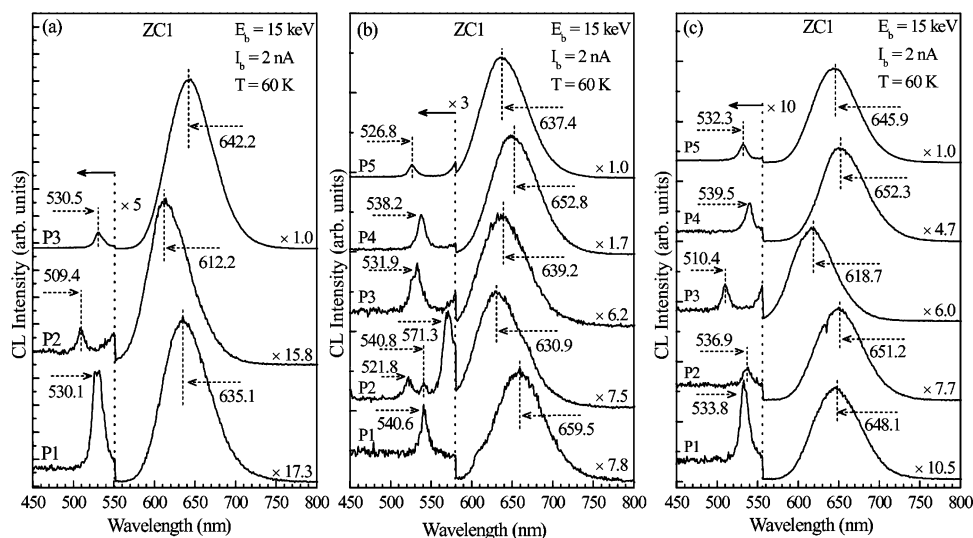


Figure 11. Local CL spectra for ZC1 at $T = 60$ K. The spectra were acquired by a focused e -beam excitation at the various points P_i shown in the monochromatic CL images of Figure 10. Each spectrum labeled as P_i in the panels a–c refer to the spots (also appropriately labeled with P_i) in the corresponding panels a–c of Figure 10. Peak positions in units of nm are indicated for the major peaks. Because of the relative weakness of the emission for the NBE peaks, an additional scaling of these peaks was performed to facilitate identification of the peak positions, as shown.

CL images gave rise to sets of sharp peaks (with full-widths at half-maximum of $\sim 15\text{--}25$ meV) centered at roughly the same wavelengths in the CL spectra. Again, this is strong evidence for an ensemble of $\text{Zn}_x\text{Cd}_{1-x}\text{Se}$ nanocrystals possessing different compositions and phases. We observed a distribution of short wavelength peaks, for example, at 486.4, 506.1, and 506.7 nm that correspond to compositions of 0.806 (c), 0.724 (c), and 0.721 (c), which are greater than the 0.69 (c) value observed in XRD. These peaks are also blue-shifted relative to the high energy peak of P6 found in the spatially integrated spectra for ZC3 in Figure 7b. Thus, large compositional undulations are evidently a factor here. Additional evidence is provided by a group of CL peaks that were located close to ~ 540 nm. The closest nominal compositions of 0.47 (h), 0.50 (c), 0.66 (h), and 0.69 (c) appearing in the XRD results would instead yield 0.556 (h) and 0.589 (c) from application of eqs (2) and (3), respectively, for $\lambda = 540$ nm. This deviation in composition ($\Delta x \approx \pm 0.07$ to ± 0.09) from the nearest values obtained in XRD is too large to account for any experimental spread in the XRD data, and thus phase separation should likely account for emission from such regions. Another important aspect of the local CL spectra for ZC3, is the nearly absent DL emission feature when spectroscopy was performed on the bright spots identified in the CL imaging results. Such behavior indicates a high crystalline quality that is evidenced by the largest quantum efficiency of luminescence for the NBE and lowest DL emission intensity relative to the other samples at all temperatures. A comparison of the luminescence efficiency at all temperatures for both NBE and DL features is presented in Figure 6 for all three samples, as noted by the relative scale factors for all features.

CONCLUSIONS

$\text{Zn}_x\text{Cd}_{1-x}\text{Se/C}$ core/shell nanocrystals were synthesized via a simple technique of pyrolyzing the solid state precursors within a sealed reactor at higher temperatures and under autogenic pressures. This method is useful in creating a carbon shell without the use of surfactants or carbon containing feedstock gas, and hence is an environmentally friendly method. The carbon shell ensures excellent surface passivation of the nanocrystals, eliminates the cytotoxicity of the nanocrystal core for biological applications, and permits adequate transparency for detecting optical activity. The nanocrystals had a 31–39 nm semiconducting core and 11–25 nm carbon shell. In the two step reactions (ZC1 and ZC2), spherical nanostructures were mostly observed, whereas a mixture of spherical and tripod nanostructures were obtained in the one-step reaction (ZC3). A mixture of three to four different cubic and hexagonal $\text{Zn}_{1-x}\text{Cd}_x\text{Se}$ phases was revealed by Rietveld analysis of the X-ray diffraction patterns of three samples,

prepared by changing the order of the reactants in the sealed reactor. The individual phases contain higher Zn content as compared to the Cd content. CL spectroscopy measurements with spatially integrated and highly localized excitations show distinct peaks and sharp lines at various wavelengths, respectively, that are likely indicative of emissions from single nanostructures possessing different compositions, phases, and sizes. XRD measurements were performed to identify the various phases and compositions, x , in the three $\text{Zn}_x\text{Cd}_{1-x}\text{Se/C}$ samples. Temperature-dependent CL spectroscopy was performed in the 60–300 K range to analyze the thermal quenching of the luminescence for both the near band-edge (NBE) and defect related emissions. The NBE emission is relatively weak in ZC1, where Zn-precursor was reacted initially followed by the Cd-precursor, as compared to ZC2 and ZC3. We attribute the measured activation energies of $\sim 50\text{--}70$ meV to reflect the presence of shallow donors or acceptors that are involved in the deep level emission for which thermal activation and quenching of the luminescence is attributed to a thermal release of electrons from shallow donors to the conduction band or a thermal release of holes from shallow acceptors to the valence band. The spatially integrated CL was analyzed by decomposing the spectra into distinct Gaussian peaks that represent emission from individual nanocrystals possessing various compositions, phases, and sizes. Some components in the CL spectra were found to be consistent with local changes in the Zn and Cd compositions caused by phase separation. The presence of the composition modulations are confirmed by the bright and dark line striations observed in the TEM images for the three samples, and provide evidence for spinodal decomposition. These composition undulations are thus reflected in the optical properties by broadening of the line shape and increasing the number of components in the luminescence spectrum. Monochromatic CL imaging at various wavelengths shows intense regions of emission that emanate from regions of reduced size, as limited by the spatial resolution of the CL technique, indicating a spatial localization of the emission in isolated single nanocrystals. Local CL spectroscopy was acquired at distinct points and compared with the results of the fits for the spatially integrated CL spectra. In addition to many sharp lines that matched the decomposed Gaussian peaks, a distribution of sharp lines was found for a given hexagonal or cubic phase and composition, again consistent with the presence of a composition modulation. These results demonstrate that details of the nanocrystal growth can lead to important consequences regarding the resulting crystalline structures (hexagonal vs cubic) present in the solid solution, as well as the relative compositions of each phase that may in turn exhibit fluctuations due to spinodal

decomposition. The simultaneous appearance of both a structural and a compositional phase separation for

the synthesis of $\text{Zn}_x\text{Cd}_{1-x}\text{Se}$ nanocrystals reveals the complexity and uniqueness of these results.

EXPERIMENTAL SECTION

Materials. Zinc acetate dihydrate [$\text{C}_4\text{H}_6\text{O}_4\text{Zn} \cdot 2\text{H}_2\text{O}$, Acros Organics, 98%], cadmium acetate dihydrate [$\text{C}_4\text{H}_6\text{O}_4\text{Cd} \cdot 2\text{H}_2\text{O}$, Aldrich, 98%], and selenium powder [100 mesh, Aldrich, 99.99%] were used as received. All the reactants were handled inside a N_2 filled glovebox.

Synthesis of ZC1. In a typical synthesis, initially 3 g of $\text{C}_4\text{H}_6\text{O}_4\text{Zn} \cdot 2\text{H}_2\text{O}$ and 2.7 g of Se were mixed well and filled inside a quartz tube fitted within a 5 mL stainless steel reactor, sealed on one end. The reactor filled with precursor was tightly sealed at the other end, heated in a tube furnace at $10^\circ\text{C min}^{-1}$, and maintained at 800°C for 10 h. The reactor was cooled (~ 5 h) to ambient temperature. The dry grayish powder was sonicated in ethanol for 30 min and dried under vacuum after decanting the dark liquid from the top to remove the contaminant carbonaceous species. The dry powder was analyzed by XRD and C, H, N analyzer that show ZnSe/C nanocrystals with 2.0% C. In the next step, 1.0 g of ZnSe/C powder was mixed with 1.3 g of $\text{C}_4\text{H}_6\text{O}_4\text{Cd} \cdot 2\text{H}_2\text{O}$ and 0.6 g Se and filled inside the sealed reactor. The sealed reactor was heat treated at 800°C for 6 h. The yield of the $\text{Zn}_x\text{Cd}_{1-x}\text{Se/C}$ product was $\sim 80\%$, based on the amount of the initial reactants and the carbon in the final products.

Synthesis of ZC2. The nanocrystals of ZC2 were again synthesized using a two step process. First, 3 g of $\text{C}_4\text{H}_6\text{O}_4\text{Cd} \cdot 2\text{H}_2\text{O}$ and 0.9 g of Se were mixed and heated inside the sealed reactor at 800°C for 10 h. The sonicated and dried product was CdSe/C , as confirmed by XRD with 3.4 wt % C. Next, 1.0 g of CdSe/C powder was reacted with 1.2 g of $\text{C}_4\text{H}_6\text{O}_4\text{Zn} \cdot 2\text{H}_2\text{O}$ and 0.5 g Se inside the sealed reactor at 800°C for 6 h to give $\sim 75\%$ yield of the $\text{Zn}_x\text{Cd}_{1-x}\text{Se/C}$ product.

Synthesis of ZC3. In a one step reaction, 2 g of $\text{C}_4\text{H}_6\text{O}_4\text{Zn} \cdot 2\text{H}_2\text{O}$, 1.8 g of $\text{C}_4\text{H}_6\text{O}_4\text{Cd} \cdot 2\text{H}_2\text{O}$, and 1.6 g of Se were reacted inside the 5 mL sealed reactor and heated at $10^\circ\text{C min}^{-1}$ until 800°C for 6 h. The product was similarly sonicated and dried under vacuum. The yield of the $\text{Zn}_x\text{Cd}_{1-x}\text{Se/C}$ product was $\sim 85\%$.

The obtained products were structurally characterized using a high resolution scanning electron microscope (HRSEM, JSM, 7000F), and transmission electron microscope (TEM, JEOL, 2010). The powder X-ray diffraction (PXRD) data were collected on a PANalytical X'Pert PRO diffractometer equipped with the PIXcel detector and the secondary graphite monochromator using $\text{Cu K}\alpha$ radiation. The composition of the products were determined with inductively coupled plasma atomic emission spectroscopy (ICP-AES; Spectroflame Module E), and energy dispersive X-ray spectroscopy (EDS, JSM, 7000F coupled to HRSEM). The cathodoluminescence (CL) experiments were performed with a modified JEOL-5910 SEM using a 15 keV electron beam with a probe current of ~ 2 nA. The system has previously been described in detail.⁴⁷ The sample was cooled with a closed-cycle liquid He system connected to the SEM sample stage by a copper braid. The sample temperature was varied from 60 to 300 K. The electron beam (e-beam) was rastered over a $64\ \mu\text{m} \times 48\ \mu\text{m}$ region during acquisition of monochromatic CL images. CL spectra acquired by locally exciting the nanocrystals (local CL spectra) were also acquired by keeping the e-beam stationary and focused on specific features. A UV multialkali photomultiplier tube (PMT) operating in the 185–850 nm spectral range enabled photon counting of the luminescence that was dispersed by a 0.25-m monochromator. The maximum spectral and spatial resolutions were ~ 0.5 nm and $\sim 0.3\ \mu\text{m}$, respectively. Each sample was prepared by transferring the as-grown material to thin strips of Cu foil, each having sizes of ca. $5\ \text{mm} \times 5\ \text{mm}$. Preparation on a metallic foil is required in order to avoid charging during the electron beam excitation of the nanocrystals in the SEM.

Supporting Information Available: X-ray dot mapping and local CL spectra and images for ZC3. This material is available free of charge via the Internet at <http://pubs.acs.org>.

REFERENCES AND NOTES

- Kim, J. I.; Lee, J. -K. *Adv. Funct. Mater.* **2006**, *16*, 2077–2082.
- Zheng, Y.; Yang, Z.; Ying, J. Y. *Adv. Mater.* **2007**, *19*, 1475–1479.
- Zhong, X.; Xie, R.; Zhang, Y.; Basché, T.; Knoll, W. *Chem. Mater.* **2005**, *17*, 4038–4042.
- Sung, Y. -M.; Park, K. -S.; Lee, Y. -J.; Kim, T. G. *J. Phys. Chem. C* **2007**, *111*, 1239–1242.
- Lim, S. J.; Chon, B.; Joo, T.; Shin, S. K. *J. Phys. Chem. C Lett.* **2008**, *112*, 1744–1747.
- Sung, Y. -M.; Lee, Y. -J.; Park, K. -S. *J. Am. Chem. Soc.* **2006**, *128*, 9002–9003.
- Talapin, D. V.; Mekis, I.; Götzinger, S.; Kornowski, A.; Benson, O.; Weller, H. *J. Phys. Chem. B* **2004**, *108*, 18826–18831.
- Mekis, I.; Talapin, D. V.; Kornowski, A.; Hasse, M.; Weller, H. *J. Phys. Chem. B* **2003**, *107*, 7454–7462.
- Qu, L.; Peng, X. *J. Am. Chem. Soc.* **2002**, *124*, 2049–2055.
- Ge, J. -P.; Xu, S.; Zhuang, J.; Wang, X.; Peng, Q.; Li, Y. -D. *Inorg. Chem.* **2006**, *45*, 4922–4927.
- Bhattacharyya, S.; Zitoun, D.; Gedanken, A. *J. Phys. Chem. C* **2008**, *112*, 7624–7630.
- Bhattacharyya, S.; Perelshtein, I.; Moshe, O.; Rich, D. H.; Gedanken, A. *Adv. Funct. Mater.* **2008**, *18*, 1641–1653.
- Geng, B. Y.; Du, Q. B.; Liu, X. W.; Ma, J. Z.; Wei, X. W.; Zhang, L. D. *Appl. Phys. Lett.* **2006**, *89*, 033115.
- Janotta, M.; Rudolph, D.; Kueng, A.; Kranz, C.; Voraberger, H. -S.; Waldhauser, W.; Mizaikoff, B. *Langmuir* **2004**, *20*, 8634–8640.
- Zhang, X. T.; Liu, Z.; Li, Q.; Hark, S. K. *J. Phys. Chem. B* **2005**, *109*, 17913–17916.
- Lee, H.; Holloway, P. H.; Yang, H.; Hardison, L.; Kleiman, D. *J. Chem. Phys.* **2006**, *125*, 164711.
- Santangelo, S. A.; Hinds, E. A.; Vlaskin, V. A.; Archer, P. I.; Gamelin, D. R. *J. Am. Chem. Soc.* **2007**, *129*, 3973–3978.
- Thuy, U. T. D.; Liem, N. Q.; Thanh, D. X.; Protière, M.; Reiss, P. *Appl. Phys. Lett.* **2007**, *91*, 241908.
- Sadofev, S.; Blumstengel, S.; Henneberger, F. *Appl. Phys. Lett.* **2004**, *84*, 3678–3680.
- Zhong, X.; Feng, Y.; Zhang, Y.; Gu, Z.; Zou, L. *Nanotechnology* **2007**, *18*, 385606.
- Charvet, N.; Reiss, P.; Roget, A.; Dupuis, A.; Grünwald, D.; Carayon, S.; Chandezon, F.; Livache, T. *J. Mater. Chem.* **2004**, *14*, 2638–2642.
- Klochikhin, A.; Reznitsky, A.; Don, B. D.; Priller, H.; Kalt, H.; Klingshirn, C.; Permogorov, S.; Ivanov, S. *Phys. Rev. B* **2004**, *69*, 085308.
- Glas, F. *J. Appl. Phys.* **1987**, *62*, 3201–3208.
- Ipatova, I. P.; Malyshkin, V. G.; Shchukin, V. A. *J. Appl. Phys.* **1993**, *74*, 7198–7210.
- Marbeuf, A.; Druilhe, R.; Triboulet, R.; Patriarche, G. *J. Cryst. Growth* **1992**, *117*, 10–15.
- Lee, H. S.; Sohn, H. S.; Lee, J. Y.; Lee, K. H.; Kim, Y. H.; Kim, T. W.; Kwon, M. S.; Park, H. L. *J. Appl. Phys.* **2006**, *99*, 093512.
- Bertram, F.; Giemisch, G.; Forster, D.; Christen, J.; Kling, R.; Kirchner, C.; Waag, A. *Appl. Phys. Lett.* **2006**, *88*, 061915.
- Zhang, X. B.; Hark, S. K. *J. Cryst. Growth* **2001**, *223*, 512–517.
- Rietveld, H. M. *J. Appl. Crystallogr.* **1969**, *2*, 65–71.
- Solovyov, L. A. *J. Appl. Crystallogr.* **2004**, *37*, 743–749.
- Rong, F.; Barry, W. A.; Donegan, J. F.; Watkins, G. D. *Phys. Rev. B* **1988**, *37*, 4329–4332.
- Rong, F. C.; Barry, W. A.; Donegan, J. F.; Watkins, G. D. *Phys. Rev. B* **1996**, *54*, 7779–7788.
- Zhu, Y.; Bando, Y. *Chem. Phys. Lett.* **2003**, *377*, 367–370.
- Xiang, B.; Zhang, H. Z.; Li, G. H.; Yang, F. H.; Su, F. H.; Wang, R. M.; Xu, J.; Lu, G. W.; Sun, X. C.; Zhao, Q.; Yu, D. P. *Appl. Phys. Lett.* **2003**, *82*, 3330–3332.

35. Zhang, X. T.; Liu, Z.; Ip, K. M.; Leung, Y. P.; Li, Q.; Hark, S. K. *J. Appl. Phys.* **2004**, *95*, 5752–5755.
36. Semenova, G. N.; Venger, Y. F.; Valakh, M. Y.; Sadofyev, Y. G.; Korsunskaya, N. O.; Strelchuk, V. V.; Borkovska, L. V.; Papusha, V. P.; Vuychik, M. V. *J. Phys.: Condens. Matter* **2002**, *14*, 13375–13380.
37. Philipose, U.; Yang, S.; Xu, T.; Ruda, H. E. *Appl. Phys. Lett.* **2007**, *90*, 063103.
38. Hernandez-Calderon I. Optical Properties and Electronic Structure of Wide Band Gap II–VI Semiconductors. In *II–VI Semiconductor Materials and Their Applications*; Tamargo M. C., Ed.; Taylor & Francis: Ann Arbor, MI, 2002.
39. Pankove, J. I. *Optical Processes in Semiconductors*; Dover Publications: New York, 1971; p 166.
40. Khatsevich, S.; Rich, D. H.; Keller, S.; DenBaars, S. P. *Phys. Rev. B* **2007**, *75*, 035324.
41. Hill, R. J. *Phys. C: Solid State Phys.* **1974**, *7*, 521–526.
42. Richardson, D.; Hill, R. J. *Phys. C: Solid State Phys.* **1972**, *5*, 821–827.
43. Richardson, D.; Hill, R. J. *Phys. C: Solid State Phys.* **1973**, *6*, L115–L119.
44. Venugopal, R.; Lin, P.-I.; Chen, Y.-T. *J. Phys. Chem. B* **2006**, *110*, 11691–11696.
45. Benosman, N.; Amrane, N.; Aourag, H. *Phys. B* **2000**, *275*, 316–327.
46. Ichino, K.; Wu, Y. -H.; Kawakami, Y.; Fujita, S.; Fujita, S. *J. Cryst. Growth* **1992**, *117*, 527–531.
47. Lin, H. T.; Rich, D. H.; Konkar, A.; Chen, P.; Madhukar, A. *J. Appl. Phys.* **1997**, *81*, 3186–3195.